



Density correlations from analog Hawking radiation in the presence of atom lossesYash Palan  and Sebastian Wüster**Department of Physics, Indian Institute of Science Education and Research, Bhopal, Madhya Pradesh 462 066, India* (Received 22 February 2022; revised 3 October 2022; accepted 1 November 2022; published 18 November 2022)

The sonic analog of Hawking radiation can now be experimentally recreated in Bose-Einstein condensates that contain an acoustic black hole. In these experiments the signal strength and approximate analog Hawking temperature increase for denser condensates, which however also suffer increased atom losses from inelastic collisions. To determine how these affect analog Hawking radiation, we numerically simulate creation of the latter in a Bose-Einstein condensate in the presence of atomic losses, including nonunitary quantum field dynamics using the truncated Wigner approximation. In particular we explore modifications of density-density correlations through which the radiation has been analyzed so far. We find no evidence that losses directly alter the basic picture of the analog Hawking effect; instead all consequences that we find are indirect: Losses increase the contrast of the correlation signal, which we attribute to condensate heating by the losses, in turn leading to a component of stimulated radiation in addition to the spontaneous one. Other indirect consequences are the modification of the white-hole instability pattern and a change of slope of the Hawking tongue.

DOI: [10.1103/PhysRevA.106.053317](https://doi.org/10.1103/PhysRevA.106.053317)**I. INTRODUCTION**

Hawking radiation [1–3] is a prominent prediction of quantum field theory in curved spacetime [4,5]. Difficulties with observing this radiation from an astrophysical black hole are a key motivation for the development of the analog gravity program [3,6,7]. The latter is founded on the mathematical correspondence between the propagation of sound in a fluid medium and the propagation of quantum fields in curved spacetime [3,8].

Applying that idea to gaseous Bose-Einstein condensates (BECs) as a quantum fluid [6,7,9,10], experiments have reported the observation of analog Hawking radiation (AHR) by measuring density-density correlations to very high precision [11–13]. Exploiting these correlations as experimental signature [14,15] offers several advantages, such as a clear connection between the Hawking particle (phonon) and its partner [14], a link to entanglement [12], the ability to discriminate AHR from other causes of particle production [16,17], and high sensitivity to an otherwise very weak signal.

Also, when observing AHR through correlations, signals are stronger when the surface gravity of the sonic black hole is larger [14]. For a fixed Mach number profile, the surface gravity increases for denser condensates. However, these are also subject to stronger atom losses [17], most notably three-body losses [18–20], the rates for which scale cubically with density. The loss channels give rise to a nonunitary component of quantum field dynamics [21], and it is not *a priori* clear if and how this alters the mechanism of AHR. For example, losses can open new wave-mixing channels in one dimension, by altering dispersion relations [22]. Losses also drive the quantum many-body state of the Bose gas away from its ground state and thus cause quasiparticle creation [23], which could

interfere with Hawking signals. Experiments reporting AHR have caused a lively debate regarding several aspects of their interpretation, such as the thermality of the spectrum [24–26], which motivates inspection of all aspects of the experimental setting, of which losses are an unavoidable one.

In this article, we numerically explore how one-, two-, and three-body losses affect AHR, in particular its correlation signals. We find no indications of any major departures from the fundamental mechanism despite the introduction of non-Hermiticity into the problem. Characteristic features in correlation functions that link sonic Hawking radiation to the black-hole horizon persist also in the presence of losses. To show this, we utilize the truncated Wigner approximation [27–30] for the dynamics of fluctuations around the mean field of a BEC, which has been successfully applied earlier in the context of analog gravity [15,31–36]. All changes in correlation signals that we can attribute to losses appear indirect, arising due to loss-induced heating or temporal changes of condensate density, rather than directly from modifications of dispersion relations. In contrast to our conjecture in Ref. [17], we find that correlation features are actually strengthened in simulations that include losses. We attribute this to an additional stimulated population in the quantum field modes responsible for Hawking radiation [37] due to loss-induced condensate heating [17,23], giving rise to the same correlation features [38,39] as the basic spontaneous radiation. Additional modifications of experimental observables by the losses are a change in the slope of the AHR tongue, the emergence of additional tongues, and the fact that patterns due to instabilities at the white hole are altered by the noise.

Our results show that the subtle interplay of multiple aspects of BEC quantum field dynamics is manifest in correlation patterns, and a careful comparison of numerical simulations and experimental results could thus also provide insight into features that are not directly pertaining to analog gravity in the future. Exchanging ideas between the analog

*sebastian@iiserb.ac.in

gravity and condensed matter communities [40], correlated emission of Hawking quanta by a sonic horizon could thus become a diagnostic to probe, e.g., dispersion relations and wave scattering.

This article is organized as follows: A brief description of the sonic black-hole scenario and the truncated Wigner method is provided in Sec. II. In Sec. III we review the correlation observable that we focus on and the most important features it exhibits. Sections therein describe the modification of these features due to atom losses, with strengthening of correlations in Sec. III A, discussion of the slope of Hawking tongues in Sec. III B, and the white-hole correlation pattern in Sec. III C. In Sec. IV we place these findings in the context of the most relevant experiment on AHR [12]. Details regarding the truncated Wigner method have been summarized in Appendixes A and B, while details regarding white-hole damping can be found in Appendix C.

II. TRUNCATED WIGNER SIMULATION OF SONIC BLACK HOLE

We consider a BEC of ^{87}Rb atoms in a one-dimensional ring trap [41,42]. Following the approach of Ref. [15] to yield tractable numerical simulations, we assume that both the external potential $V(x, t)$ and the interaction strength $U_0(x, t)$ can be varied as a function of the coordinate x along the ring and in time, t . For atoms of mass m the Gross-Pitaevskii equation (GPE) [43] that describes the dynamics of the mean field $\psi(x, t)$ is then

$$i\hbar \frac{\partial \psi}{\partial t} = \left[-\frac{\hbar^2}{2m} \frac{\partial^2}{\partial x^2} + V(x, t) + U_0(x, t) |\psi|^2 \right] \psi. \quad (1)$$

For time $t < 0$, we assume that the interaction strength is constant in space, $U_0(x) = U_{\text{ini}}$, and there is no external trapping potential, $V = 0$. In this case,

$$\psi(x, t < 0) = \sqrt{\rho_0} e^{ik_0 x}, \quad (2)$$

with density ρ_0 and condensate flow velocity $v_0 = \hbar k_0 / m$ related to the wave number k_0 , is a solution of the time-independent GPE and thus a steady state of Eq. (1). At $t = 0$, we assume the interaction and external potential are modified (quenched) to

$$V(x, t > 0) = \begin{cases} V_{\text{sub}} + \frac{(V_{\text{sup}} - V_{\text{sub}}) [\tanh(\frac{x-x_h}{\sigma_{sp}}) + 1]}{2}, & x < 0 \\ V_{\text{sup}} - \frac{(V_{\text{sup}} - V_{\text{sub}}) [\tanh(\frac{x-x_w}{\sigma_{sp}}) + 1]}{2}, & x > 0, \end{cases} \quad (3)$$

with x_h the target location of the black-hole horizon, x_w the white-hole horizon, and σ_{sp} the length scale of the smoothed step function, shown also in Fig. 1(a). Choosing further a constant combination

$$U_{\text{sub}} \rho_0 + V_{\text{sub}} = U_{\text{sup}} \rho_0 + V_{\text{sup}} \equiv C, \quad (4)$$

we obtain the variation of the interaction strength $U_0(x, t > 0)$ as

$$U_0(x, t > 0) = \frac{C - V(x, t > 0)}{\rho_0}. \quad (5)$$

This makes sure the chemical potential $\mu = \hbar^2 k_0^2 / (2m) + V_{\text{sub}} + U_{\text{sub}} \rho_0$ is constant and thus preserves Eq. (2) as a solu-

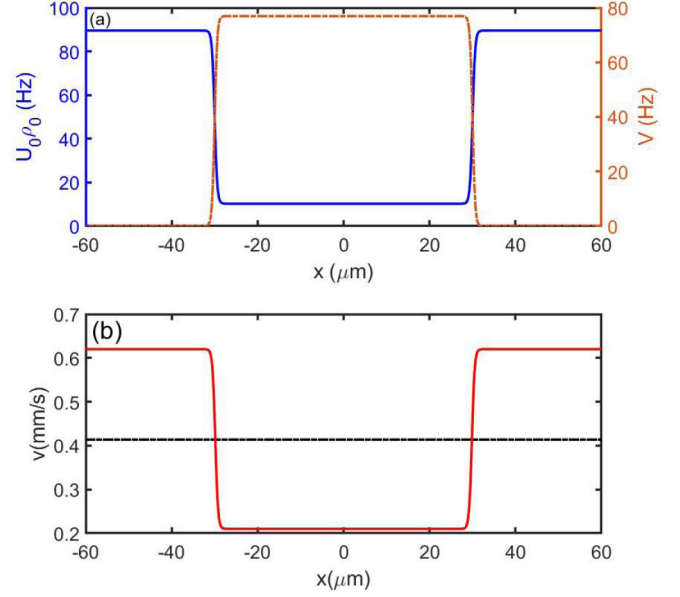


FIG. 1. Potential, interaction, and flow profiles of a BEC in a periodic one-dimensional (1D) domain (on a ring). The ring is divided into two regions by the black-hole horizon, at $x_h = -30 \mu\text{m}$ and the white-hole horizon, at $x_w = 30 \mu\text{m}$. (a) Shape of the external potential $V(x)$ in Eq. (3) (orange dashed line) and interaction strength $U_0(x)$ in Eq. (5) (blue line) at times $t > 0$ with $V_{\text{sub}} = 0$, $U_{\text{sub}} = c_{\text{sub}}^2 m / \rho_0$, and $U_{\text{sup}} = c_{\text{sup}}^2 m / \rho_0$ indicated as text. V_{sup} is calculated using Eq. (4). The width of the step is $\sigma_{sp} = 0.6 \mu\text{m}$. (b) The spatial variation of the speed of sound, $c_s(x)$ (solid red line), with $c_{\text{sub}} = 0.62 \text{ mm/s}$ and $c_{\text{sup}} = 0.21 \text{ mm/s}$, and velocity of the condensate v_0 (black dashed line) for $t > 0$.

tion of the time-independent GPE, albeit now an unstable one. This allows us to focus on the quench dynamics of quantum fluctuations around the mean field, without distractions by mean-field dynamics.

The choice of potential divides the ring into a subsonic region, where $v_0 < c_s(x) = \sqrt{U_0(x) \rho_0 / m}$, with speed of sound c_s , and a supersonic region where $v_0 > c_s(x)$. The transition from the subsonic to the supersonic region along the flow direction marks the black-hole horizon, while the reverse marks the white-hole horizon. Accordingly the interaction strength and external potential in Eqs. (3) and (5) have been marked by subscripts {sub, sup}, with “sub” referring to the subsonic region and “sup” referring to the supersonic region. The change of parameters described causes a sudden quench, from a flat analog spacetime in a condensate without flow variation, to a spacetime containing a black-hole-white-hole pair, in a condensate with trans-sonic flow [44,45]. Note that, while it is in principle realizable, the transition scheme from subsonic to supersonic flow discussed above has been chosen for numerical convenience only. In practice, one would require a spatial dependence of the interaction strength by exploiting a Feshbach resonance with an inhomogeneous magnetic field, an accordingly tuned external potential $V(x)$, e.g., optically, while working in a toroidal trap. It is experimentally much more straightforward to use a straight cigar-shaped trap, in which the subsonic-to-supersonic transition occurs due to joint density and velocity variations induced by the external

potential $V(x, t)$ only, keeping U_0 constant. This has hence been used in the actual experiment [12]. We expect all our results to pertain also to that scenario, and make more direct contact with at least all parameters used there in Sec. IV.

To numerically model AHR, we need to include quantum fluctuations of the condensate. This is done in the truncated Wigner approximation (TWA) [27–30]. In the TWA method, the quantum state is represented by an ensemble of stochastic trajectories, with initial state given by

$$\psi(x, 0) = e^{ik_0x} \left[\sqrt{\rho_0} + \sum_{k \neq 0} \beta_k u_k e^{ikx} - \beta_k^* v_k e^{-ikx} \right], \quad (6)$$

where β_k is a complex Gaussian random variable with $\overline{\beta_k} = \overline{\beta_k^*} = 0$ and $\overline{\beta_k \beta_{k'}} = \delta_{kk'} [2 \tanh(\epsilon_k / 2k_b T)]^{-1}$. Here, $\overline{\dots}$ denotes the stochastic average and T is the temperature of the Bose gas. The Bogoliubov coefficients u_k and v_k are defined as usual in terms of the kinetic energy $E_k = \frac{\hbar^2 k^2}{2m}$ and $\epsilon_k = \sqrt{E_k(E_k + 2U_0 \rho_0)}$ according to $u_k \pm v_k = (E_k / \epsilon_k)^{\pm 1/2}$.

The above stochastic initial state is then evolved using the TWA equation of motion, which follows from the master equation that includes atomic ($\ell = 1, 2, 3$)-body loss [21,23]:

$$\frac{d\hat{\rho}}{dt} = -\frac{i}{\hbar} [\hat{H}, \hat{\rho}] + \sum_{\ell=1}^3 \gamma_{\ell,1D} \int dx \mathcal{D}[\hat{\Psi}^\ell] \hat{\rho}, \quad (7)$$

where $\mathcal{D}[\hat{a}] \hat{\rho} \equiv \hat{a} \hat{\rho} \hat{a}^\dagger - \hat{a}^\dagger \hat{a} \hat{\rho} / 2 - \hat{\rho} \hat{a}^\dagger \hat{a} / 2$, \hat{H} is the usual Hamiltonian giving rise to Eq. (1), and $\gamma_{\ell,1D}$ is the ℓ -body loss rate after reduction to one dimension (see Appendix D).

We distinguish three major loss types in a BEC, depending on their scaling with density, arising through a variety of different mechanisms each: (i) one-body loss of the condensate atoms due to stray photons or vacuum imperfections; (ii) two-body loss, involving atomic collisions and hence dependent on density, which can arise through spin flipping two-body interactions or light assisted collisions; and (iii) three-body losses, due to inelastic collisions causing two atoms to form a molecule, which requires a third spectator to balance conservation laws and leads to the loss of all three involved condensate atoms [46].

We find the TWA equations of motion from Eq. (7) with the help of replacement rules [27] following Ref. [47] (see Appendix A). The final result is

$$\begin{aligned} d\psi(x, t) &= dL_1 + dL_2 + dL_3 \\ &- \frac{i}{\hbar} \left[-\frac{\hbar^2}{2m} \frac{\partial^2}{\partial x^2} + V(x, t) + U_0(x, t) |\psi(x, t)|^2 \right] \\ &\times \psi(x, t) dt, \end{aligned} \quad (8)$$

where decay and noise terms dL_k for k -body loss are

$$dL_1 = -\gamma_{1,1D} \psi dt + \sqrt{\gamma_{1,1D}} d\mathcal{W}, \quad (9a)$$

$$dL_2 = -\gamma_{2,1D} |\psi|^2 \psi dt + 2\sqrt{\gamma_{2,1D}} |\psi| d\mathcal{W}, \quad (9b)$$

$$dL_3 = -\frac{\gamma_{3,1D}}{2} |\psi|^4 \psi dt + \frac{\sqrt{3\gamma_{3,1D}}}{\sqrt{2}} |\psi|^2 d\mathcal{W}. \quad (9c)$$

Here $\gamma_{1,1D}$, $\gamma_{2,1D}$, and $\gamma_{3,1D}$ are the effective one-body, two-body, and three-body loss coefficients in one dimension, respectively (see Appendix A). The symbol

$d\mathcal{W} = d\mathcal{W}(x, t)$ denotes complex standard Wiener noise, with correlations $\overline{d\mathcal{W}(x, t)} = 0$, $\overline{d\mathcal{W}(x, t) d\mathcal{W}(x', t')} = 0$, and $\overline{d\mathcal{W}(x, t) d\mathcal{W}^*(x', t')} = \delta(x - x') \delta(t - t') dt$.

Finally, quantum field observables are extracted using symmetrically ordered averages [27], such that, for example, the total atomic density is

$$\langle \hat{\Psi}^\dagger(x) \hat{\Psi}(x) \rangle = \overline{|\psi(x)|^2} - \frac{1}{2} \delta_p(x, x), \quad (10)$$

where for a spatial domain $-L \leq x < L$ the expression

$$\delta_p(x, x') = \frac{1}{L} \sum_k [u_k^2 e^{ik(x-x')} - v_k^2 e^{-ik(x-x')}] \quad (11)$$

is a restricted basis commutator, discussed in Appendix B. It has been shown in Ref. [47] that the truncation restricts the validity of the TWA method to scenarios where $|\psi(x)|^2 \gg \delta_p(x, x)$. More details regarding the TWA method can be found in Ref. [30]. It has been demonstrated first in Ref. [14] that the creation of analog Hawking radiation can be modeled using the TWA.

III. DENSITY CORRELATIONS

One of the most straightforward manifestations of AHR, considered in early works on analog gravity [48], would be the reheating of the condensate to the analog Hawking temperature,

$$T_H = \frac{\hbar g_h}{2\pi k_b c_h}, \quad \text{with } c_h = c_s(x_h), \quad (12)$$

where c_s is the speed of sound, v_0 is the velocity of the condensate, x_h is the location of the black-hole horizon, and g_h the surface gravity of the sonic black hole. The last can be found from [14,45]

$$g_h = \frac{1}{2v_0} \left. \frac{d[c^2(x) - v^2(x)]}{dx} \right|_{x=x_h}. \quad (13)$$

Demonstrating AHR thermally in this manner would, however, not be practical, as the temperature is fundamentally limited by atomic loss processes [16] and remains less than the equilibrium temperature of loss-induced heating [17]. More importantly, it has since been realized that the nonphononic part of the Bogoliubov spectrum causes significant deviations from a thermal spectrum [25,49], although correlated emission of quanta persists for all frequencies with a horizon [50].

A popular observable that circumvents these problems is the density-density correlation function [14]:

$$G_2(x, x') = \frac{\langle \hat{\Psi}^\dagger(x) \hat{\Psi}^\dagger(x') \hat{\Psi}(x) \hat{\Psi}(x') \rangle}{\langle \hat{\Psi}^\dagger(x) \hat{\Psi}(x) \rangle \langle \hat{\Psi}^\dagger(x') \hat{\Psi}(x') \rangle}. \quad (14)$$

Density-density correlations $G_2(x, x')$ appear between a location x outside the horizon and another one, x' , inside the horizon, since the Hawking particle and its antiparticle are created from the same entangling event at the event horizon. In contrast, preexisting thermal excitations or those induced by losses are not expected to share any correlations that are linked to the horizon.

The experiments [12,13] thus relied on correlations (14) as a signature for AHR. The TWA method provides symmetrically ordered quantum correlations via averages of the

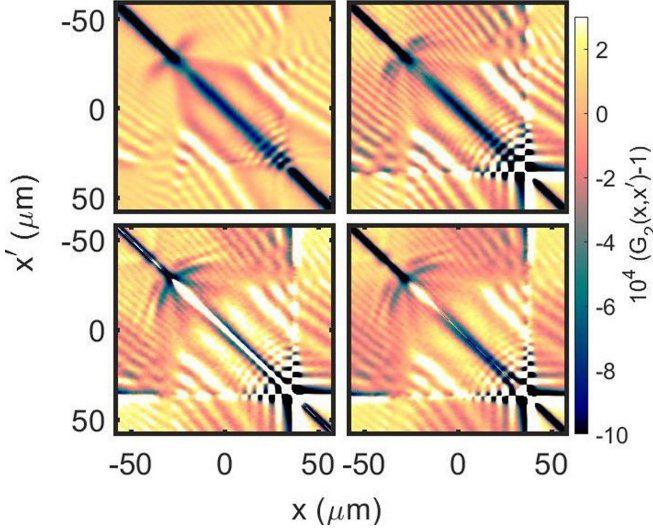


FIG. 2. Density-density correlations $G_2(x, x') - 1$ near a sonic horizon (at $x = -30 \mu\text{m}$), including (a) no loss, (b) only one-body loss, (c) only two-body loss, and (d) only three-body loss. We show snapshots at $t = 48 \text{ ms}$ after the initial quench. Movies for the same scenarios can be found in the Supplemental Material [51]. The features indicated by numbered arrows are discussed in the text.

stochastic wavefunction [3,27], which gives us the numerator of Eq. (14) as

$$\begin{aligned} & \langle \hat{\Psi}^\dagger(x) \hat{\Psi}^\dagger(x') \hat{\Psi}(x) \hat{\Psi}(x') \rangle \\ &= \overline{|\psi(x)|^2 |\psi(x')|^2} - \frac{1}{2} \overline{|\psi^*(x) \psi(x') \delta_p(x, x')|} \\ & \quad + \overline{|\psi^*(x') \psi(x) \delta_p(x', x)|} + \overline{|\psi(x)|^2 \delta_p(x', x')} \\ & \quad + \overline{|\psi(x')|^2 \delta_p(x, x)} + \frac{1}{4} [\delta_p(x, x) \delta_p(x', x')] \\ & \quad + \delta_p(x, x') \delta_p(x', x)]. \end{aligned} \quad (15)$$

The elements of the denominator can be calculated from Eq. (10).

In this article, we compare the correlation signatures of AHR with and without the inclusion of atomic losses. These are shown in Fig. 2, using $N_{\text{traj}} = 2 \times 10^5$ stochastic trajectories, i.e., solutions of Eq. (8) at zero temperature, $T = 0$. The condensate flow velocity is $v_0 = 0.415 \text{ mm/s}$, with speed of sound in the subsonic and supersonic regions $c_{\text{sub}} = 0.62 \text{ mm/s}$ and $c_{\text{sup}} = 0.21 \text{ mm/s}$, respectively, roughly matching conditions of Ref. [12]. The circumference of our ring or length of the 1D domain is chosen as $L = 60 \mu\text{m}$, and the mean density prior to the quench at $t < 0$ used in the simulations is $\rho_0 = 66.6 \mu\text{m}^{-1}$. Finally, the three-dimensional (3D) loss coefficients were set to $\gamma_{1,3D} = 3.096 \text{ s}^{-1}$, $\gamma_{2,3D} = 0.39 \mu\text{m}^3/\text{s}$, $\gamma_{3,3D} = 0.06 \mu\text{m}^6/\text{s}$. These values for $\gamma_{1,3D}$ and $\gamma_{3,3D}$ are slightly larger than typical, since we have chosen them here as the minimal ones for which correlation patterns in the presence of each loss type separately differ from those without losses on a 50-ms time scale. We will discuss the scenario with more typical rates for all three loss channels in Sec. IV.

Loss rates were then converted to the effective 1D loss rates using Eq. (D6), by assuming a transverse trapping frequency of $\omega_\perp / (2\pi) = 130 \text{ Hz}$. Solutions of Eq. (8) and averages (14)

are obtained using the high-level language XMDS [52]. To smoothen the correlations, they have been convolved with a Gaussian filter with kernel width $\approx 1.7 \mu\text{m}$.

Let us first describe the features in the correlation function $G_2(x, x')$ for the basic scenario without losses in Fig. 2(a), which have been observed before [15,35]:

(1) The strip of correlations $G_2(x, x') < 1$ near the diagonal, $x = x'$, appears due to atomic antibunching induced by repulsive interactions [15,53]. This allows us to verify the sampling of correlations by comparing the antibunching feature obtained with that from analytical calculations.

(2) The pattern of fringes that run parallel to the diagonal and propagate away from it in time are a result of the interaction quench between $t = 0 \text{ ms}$ and $t = 2 \text{ ms}$. These are due to the dynamical Casimir effect [15,54], similar to cosmological particle creation [10,55].

(3) The two tongues, which emerge from the diagonal at the location $(x, x') = (x_h, x_h)$, with $x_h \approx -30 \mu\text{m}$ corresponding to the sonic black-hole horizon, are the key signature of analog Hawking radiation in the density-density correlation function [14,15]. These tongues indicate correlation between the two points x and x' on either side of the horizon, due to the presence of the Hawking particle and antiparticle analogs at x and x' .

Our central observation is that these features are not dramatically altered despite the quantum field evolution becoming nonunitarity due to loss channels, suggesting that the basic mechanism of analog Hawking radiation is unchanged by this qualitative modification. However, in Figs. 2(b)–2(d), we have also marked newly appearing features of interest 4 and 5 (and changes to 3), through which results for the case with atomic losses deviate quantitatively from the loss-free scenario. These constitute our main results, and are discussed in the subsequent sections.

A. Stronger correlations in the presence of loss

We find that the contrast of the Hawking tongues *increases* with the inclusion of loss in the simulation, pertaining to feature 3 or feature 4 in Fig. 2(d), the opposite effect to what was our conjecture in Ref. [17]. To see the effect more clearly, we show one-dimensional cuts of the correlations along the tongue in Fig. 3(a), comparing simulations with all three types of loss.

To understand the physical reason for the increase of contrast, recall that Hawking radiation can also be stimulated [37], in the cosmological as well as in analog systems, instead of being emitted spontaneously [12]. Bogoliubov modes involved in stimulated AHR are identical to those responsible for spontaneous AHR; hence both processes give rise to the same correlation patterns, as has been observed experimentally [38,39]. Since one consequence of atom losses is heating of the condensate to a temperature $T_{\text{loss}} = mc^2/2$ [23], the strengthening of correlations can be linked to this heating.

To corroborate this, we first inspect the momentum spectrum (and thus Bogoliubov excitation spectrum) of the stochastic field, for simulations without flow and no horizon, but starting with the same initial density as in Fig. 3. For $k_0 = 0$, we find from Eq. (6) that the momentum density at

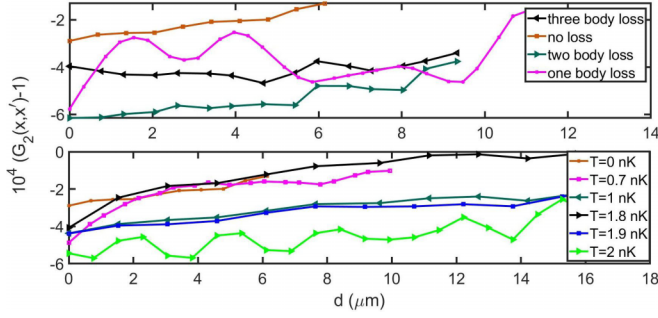


FIG. 3. Correlation signal $G_2(x, x') - 1$ as a function of the distance d from the diagonal ($x = x'$) on a 1D cut along the Hawking tongues, marked as features 3 and 4 in Fig. 2. In (a) we vary the type of loss added as shown in the legend, and in (b) we vary the initial temperature of the condensate, while not including loss. Both panels are for time $t = 48$ ms. The sampling error for $N_{\text{traj}} = 2 \times 10^5$ trajectories is not visible on the scale of the figure.

$|k| > 0$ is given by

$$\begin{aligned} n_T(k) &= \overline{\tilde{\psi}^*(k)\tilde{\psi}(k)} - \tilde{\delta}_c(k, k)/2 \\ &= (|u_k|^2 + |v_k|^2) \frac{1}{e^{-\epsilon_k/(k_B T)} - 1} + |v_k|^2, \end{aligned} \quad (16)$$

for a BEC in equilibrium at temperature T . Here $\tilde{\psi}(k)$ is the Fourier transform of $\psi(x, 0)$. By fitting this form into spectra from the simulation, we demonstrate in Fig. 4 that the loss can already significantly heat the condensate towards T_{loss} on the short time scale $t^* = 48$ ms pertaining to Fig. 3. We show $n(k, t) = \overline{\tilde{\psi}^*(k, t)\tilde{\psi}(k, t)} - \tilde{\delta}_c(k, k)/2$ at $t = t^*$ sampled from the stochastic wavefunction (black lines), together with $n_T(k)$ expected from Eq. (16) for the initial vacuum at $T = 0$ (blue dashed lines) and for the final heated quasiequilibrium [56] state at $T = T_{\text{loss}}$ (red dashed lines). In the simulations, the momentum density $n(k, t)$ starts out on the blue line at $t = 0$ and then dynamically approaches the red line due to heating.

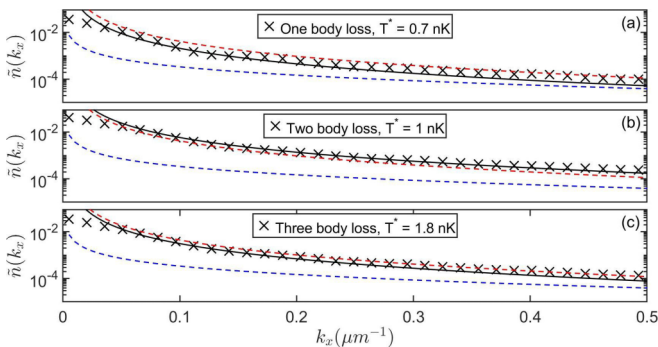


FIG. 4. Nonequilibrium heating $n(k, t^*)$ due to loss by time $t^* = 48$ ms (black lines), for the scenario as in Fig. 3 but without flow or horizon, considering (a) one-body loss, (b) two-body loss, and (c) three-body loss, with rates as used for Fig. 3. We also show the initial vacuum population as a blue dashed line, and $n_{[T_{\text{loss}}]}(k)$ from Eq. (16) as a red dashed line. The nonequilibrated spectrum roughly matches (a) $T^* = 0.7$ nK, (b) $T^* = 1.8$ nK, and (c) $T^* = 1$ nK, shown by \times . The sampling error is not visible on the scale of the figure.

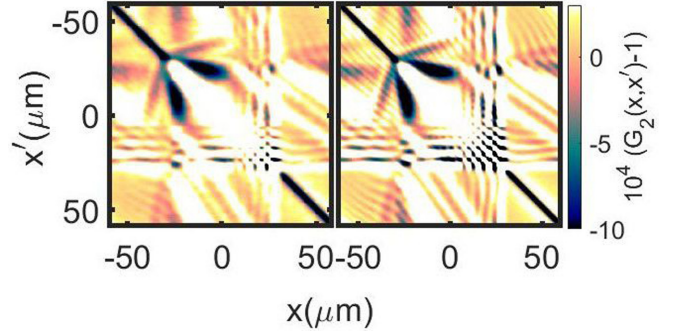


FIG. 5. Density-density correlations near a sonic horizon at $x, x' \approx x_h = -30 \mu\text{m}$, for nonvanishing initial temperatures (a) $T = 1.9$ nK and (b) $T = 2$ nK at time $t = 48$ ms, but not including dynamical loss processes.

For larger times t than shown here (and not too strong loss rates), phonon excitations saturate on the red dashed line. They can slightly overshoot, as in Fig. 4(b), if loss rates are larger. For the shorter time t^* , relevant to Fig. 3, heating is mostly incomplete and the spectrum not yet thermal. We can nonetheless satisfactorily fit a large range of wavenumbers using a temperature $T^* = 0.7$ nK, 1.8 nK, and 1 nK for one-, two-, and three-body loss, respectively.

For a final verification whether the temperatures inferred in Fig. 4 can give rise to the level of correlation modification shown in the top panel of Fig. 3, we show simulations in the bottom panel of Fig. 3 where we start at the corresponding nonzero temperatures $T \neq 0$ initially, but remove loss processes. These cases should give rise to a larger fraction of stimulated AHR, since in these the Bose gas contains phonon excitations already from the beginning. We see that temperatures inferred from Fig. 4 already give rise to a qualitatively compatible increase of correlations, while for a quantitative one slightly higher temperatures would be required. For example, the signal including three-body loss in Fig. 3(a) lies in between the results for $T = 1.9$ nK and $T = 2$ nK, with some deviation in details. Note, however, that a more rigorous discussion should be based on Bogoliubov–de Gennes (BdG) modes in the presence of the horizon for quantifying loss heating, which is challenging.

We also show the entire correlation function for nonzero initial temperatures $T = 1.9$ nK and $T = 2$ nK, but excluding losses in Fig. 5. The closer resemblance of the Hawking tongues including losses in Figs. 2(b)–2(d) with the ones in Fig. 5 compared to Fig. 2(a) again strengthens the association of signal increase with heating-induced losses. Simulations of AHR with a finite initial temperature were also presented in Ref. [15], demonstrating two tongues, the one due to spontaneous AHR and a second one due to the reflection of thermal phonons off the horizon. This is similar to what we observe in Figs. 2(b), 2(c), and 2(d) at the black-hole horizon near (x_h, x_h) .

B. Change of slope in presence of loss

Along with an increase in the strength of the Hawking tongues, we notice in Figs. 2(b)–2(d) a change of the slope in the x, x' plane of the Hawking tongue, marked feature

4. This slope α is dynamically constrained by the propagation velocity of the correlated Hawking phonons in the moving medium that they are immersed in, and is computed as $\alpha = \frac{v_0 - c_{\text{sub}}}{v_0 - c_{\text{sup}}} = 1$ for the region $x > x'$, in the scenario of Fig. 2(a) [15].

We can attribute the variation of the slope to the decrease in the speed of sound in both regions, since loss dynamically reduces the density of the system. This leads to a decrease in $|v_0 - c_{\text{sub}}|$, since c_{sub} reduces from its original value to become closer to v_0 , while $|v_0 - c_{\text{sup}}|$ increases, as c_{sup} decreases from its original value to drop further below v_0 . Hence, $\alpha = \frac{v_0 - c_{\text{sub}}}{v_0 - c_{\text{sup}}}$ decreases in magnitude, which is what we observe in Figs. 2(b)–2(d), where the tongues bend inwards towards the diagonal. As an example, for Fig. 2(d), the mean density has decreased by 36.2% when compared to the mean density at $t = 0$ ms, decreasing c_{sup} by a factor of ≈ 1.21 and c_{sub} by ≈ 1.19 .

In principle, the variation of the two speeds of sound causes the slope of the Hawking tongue to change in time, hence it should be curved. However, this curvature is small and hence the Hawking tongue can be well approximated by a line, justifying our use of linear cuts for Fig. 3.

C. White hole correlation pattern

Let us now discuss feature 5 in Fig. 2(d). It is known that the system with a black-hole (BH) and white-hole (WH) horizon is dynamically unstable, forming a black-hole laser [57,58] through the exponential amplification of the superluminal partners of analog Hawking radiation bouncing back and forth between the horizons. The checkerboard pattern visible near the white hole ($x_w = 3 \mu\text{m}$) in Fig. 2(a) has earlier been attributed to unstable modes of the white hole [32,34]. Separating the BH and the WH, it has been shown that it is the WH that causes the instabilities [59].

We see here that atomic losses strengthen the checkerboard pattern [compare Fig. 2(a) with Fig. 2(d)]. Our interpretation is again that this is due to loss-induced heating, which creates noise that seeds these instabilities more strongly than the pure vacuum fluctuations in Eq. (6). To demonstrate that the pattern can be attributed to white-hole instabilities, we show in Fig. 6(b) the scenario where strong damping is present at the white hole, which removes the pattern. The density for this scenario is shown in Fig. 6(a), together with the damping kernel. Further details about the damping potential can be found in Appendix C. Our simulations indicate that any thermal excitation or heating of a condensate containing a white hole must be taken into account when probing instabilities of the white-hole flow, also if that forms part of a black-hole laser. Loss should thus be included when attempting to establish to what extent standing wave patterns and correlations in the black-hole lasing experiment [11] are due to kinetic effects [60], number fluctuations [36], or self-amplified Hawking radiation [11,26].

IV. DISCUSSION OF EXPERIMENTS

Our article so far outlined basic mechanisms based on which dynamical loss of atoms can affect correlation signa-

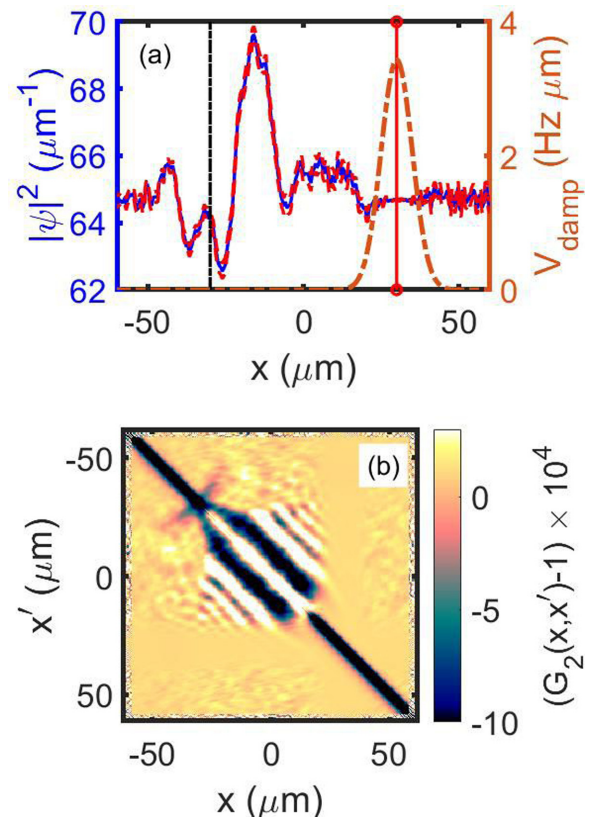


FIG. 6. (a) Spatial variation of condensate density (blue) and damping potential (orange), as defined in Eq. (C1). The black vertical line represents the black-hole horizon while the red represents the white-hole horizon. (b) Correlation pattern $G_2(x, x') - 1$ in the presence of strong damping at the white hole. The simulation is for a BEC with no losses at $T = 0$ nK.

tures of Hawking radiation, in general. In this section we will discuss these mechanisms in the context of the experiment [12] conducted on analog Hawking radiation in a BEC. We defer a detailed TWA modeling of the experimental sequence with losses to a future publication (see also Ref. [36]). A thorough assessment of loss heating for that scenario requires an accurate initial state, such as obtained from BdG modes using the self-consistent Hartree-Fock-Bogoliubov equations, going beyond the scope of the present article. Instead, we provide qualitative statements based on our findings here. Background density, flow velocity, atomic species, transverse trapping (and thus 1D interaction strengths), and spatial scale of velocity variation at the horizon used in Sec. III are already chosen based on the experiment [12]. However, the loss rates were adjusted to the lowest ones for which the correlation pattern begins to visibly deviate from the loss-free scenario. We now take $\kappa_3 = 2 \times 10^{-41} \text{m}^6 \text{s}^{-1}$ [61]. One- and two-body losses depend on experimental details such as vacuum properties and trapping light; hence we simply set them such that the corresponding atom loss is possibly significant but would not be a dominant factor in the experiment. For $\kappa_1 = 5 \times 10^{-1} \text{s}^{-1}$ and $\kappa_2 = 8 \times 10^{-20} \text{m}^3 \text{s}^{-1}$ the condensate in our simulations loses only $\sim 5\%$ of the atoms each until the time of interest, $t^* = 48$ ms.

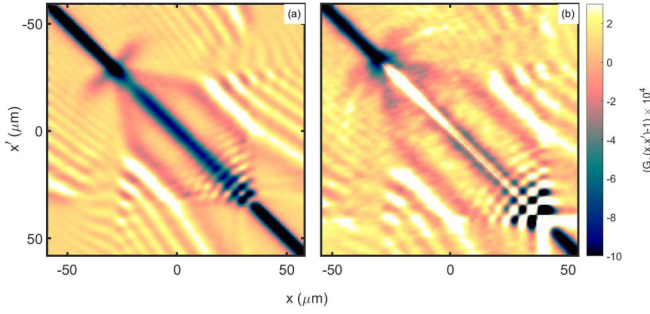


FIG. 7. Impact of loss on correlations for parameters closely resembling the experiment in Ref. [12], albeit using the present simplified trapping scenario. (a) Loss-free case, identical to Fig. 2(a) and shown for ease of comparison. (b) Correlations in the simultaneous presence of one-, two-, and three-body losses with rates given in the text.

For these parameters we compare correlations of the loss-free scenario with those in the presence of all three channels in Fig. 7. The latter shares features that we identified for the separate channels in Fig. 2, albeit more weakly. Overall the pattern is affected, but not dramatically so.

Losses now cause a reduction of about $\sim 9.9\%$ of the initial density during $t^* = 48$ ms, accordingly lowering the upstream speed of sound in the experiment by 5%. Assuming the downstream speed of sound is not affected due to the much lower condensate density in that region, this can cause a dynamic change of the expected slope of the Hawking tongue by $\sim 20\%$. In particular this could cover an inconsistency of about 5–10 % reported in Ref. [62] between the experimentally observed slope and that expected from the separate density measurement.

V. CONCLUSIONS AND OUTLOOK

We have modeled the effect of atom loss in a Bose-Einstein condensate on the correlation signature of analog Hawking radiation. For this we used the truncated Wigner approximation to include the dynamics of fluctuations around the mean field. We find that the contrast of the main correlation signal increases due to losses. We attribute this to the additional presence of stimulated Hawking radiation. The latter is an indirect effect, in which the condensate first heats up due to the losses [17,23], and thermally populated fluctuations subsequently stimulate AHR [63]. Another consequence of the same heating effect is a strengthening of the white-hole instability pattern. Through the density reduction, the loss additionally leads to a change of slope of the Hawking tongue.

Our results indicate that measurements of AHR correlations can provide information on additional processes in the Bose gas, not directly linked to AHR, and that spurious stimulated contributions should be taken into account when interpreting experiments. In a next step, it would be interesting to study the effect of losses on entanglement of the Hawking quanta. This has been studied based on a modified Peres-Horodecki criterion [64,65] to assess the nonseparability of the output state [66], Gaussian contangles [67], logarithmic negativities [50], and through the violation of

Cauchy-Schwarz inequalities [68–70]. Environmental effects such as losses or heating often degrade entanglement [71], while it has been shown to persist at finite temperature to some extent [70]. It would thus be interesting to assess whether the strengthening of correlations by the effects reported here extends to quantum correlations.

Some of our results may pertain also to sonic black holes in exciton-polariton condensates [72–75], where loss balanced by driving noise is not an undesired side effect, as in atomic BECs, but an essential feature of the setup.

ACKNOWLEDGMENTS

We gladly acknowledge fruitful discussions with A. Pendse, A. Sreedharan, and A. Rana. Financial support from the Max-Planck society under the MPG-IISER partner group program is also gratefully acknowledged.

APPENDIX A: TRUNCATED WIGNER TREATMENT OF LOSSES

We now briefly describe the origin of Eqs. (9a), (9b), and (9c), with more details available in, e.g., Refs. [30,47].

For this purpose we consider the evolution equation due to three-body losses [47]. The master equation for the three-body recombination process, in the Schrödinger picture, is [23]

$$\frac{\partial \hat{\rho}}{\partial t} = -\frac{i}{\hbar} [\hat{H}, \hat{\rho}(t)] + \frac{\gamma_{3,1D}}{6} \int dx [2\hat{\Psi}(x)^3 \hat{\rho} \hat{\Psi}^\dagger(x)^3 - \hat{\Psi}^\dagger(x)^3 \hat{\Psi}(x)^3 \hat{\rho} - \hat{\rho} \hat{\Psi}^\dagger(x)^3 \hat{\Psi}(x)^3], \quad (\text{A1})$$

where

$$\hat{H} = \int dx \left[\hat{\Psi}^\dagger(x) \left\{ -\frac{\hbar^2}{2m} \frac{\partial^2}{\partial x^2} + V(x) \right\} \hat{\Psi}(x) + \frac{U_0}{2} \hat{\Psi}^\dagger(x) \hat{\Psi}^\dagger(x) \hat{\Psi}(x) \hat{\Psi}(x) \right]. \quad (\text{A2})$$

We can express the density matrix $\hat{\rho}$ in terms of the Wigner function $W(\psi, \psi^*)$ as [30]

$$W(\psi(x), \psi^*(x)) \equiv \frac{1}{\pi^2} \int D[\lambda(x)] D[\lambda^*(x)] \times \exp(-\lambda(x)\psi^*(x) + \lambda^*(x)\psi(x)) \chi_w(\lambda(x), \lambda^*(x)), \quad (\text{A3})$$

where $D[\lambda(x)]$ is a functional integration, and the characteristic function $\chi_w(\lambda(x), \lambda^*(x))$ is given by [30]

$$\chi_w(\lambda(x), \lambda^*(x)) = \text{Tr} \left[\hat{\rho} \exp \left\{ \int dx (\lambda \hat{\Psi}^\dagger(x) - \lambda^* \hat{\Psi}(x)) \right\} \right]. \quad (\text{A4})$$

One then converts the equation of motion (A1) for the density operator into an equation of motion for the Wigner function. By computing the functional derivatives of the displacement operator,

$$\hat{D} \equiv \exp \left\{ \int dx (\lambda(x) \hat{\Psi}^\dagger(x) - \lambda^*(x) \hat{\Psi}(x)) \right\}, \quad (\text{A5})$$

with respect to $\lambda(x)$ and λ^* , and considering the effect of the same on the equation of motion of the Wigner function,

one arrives at the functional Wigner operator correspondences [27]:

$$\hat{\Psi}(x)\hat{\rho} \rightarrow \left[\psi(x) + \frac{1}{2} \frac{\delta}{\delta\psi^*(x)} \right] W(\psi, \psi^*, t), \quad (\text{A6a})$$

$$\hat{\rho}\hat{\Psi}^\dagger(x) \rightarrow \left[\psi^*(x) + \frac{1}{2} \frac{\delta}{\delta\psi(x)} \right] W(\psi, \psi^*, t), \quad (\text{A6b})$$

$$\hat{\rho}\hat{\Psi}(x) \rightarrow \left[\psi(x) - \frac{1}{2} \frac{\delta}{\delta\psi^*(x)} \right] W(\psi, \psi^*, t), \quad (\text{A6c})$$

$$\hat{\Psi}^\dagger(x)\hat{\rho} \rightarrow \left[\psi^*(x) - \frac{1}{2} \frac{\delta}{\delta\psi(x)} \right] W(\psi, \psi^*, t). \quad (\text{A6d})$$

The resultant equation of motion for W when including losses will contain up to third-order partial derivatives with respect to ψ and ψ^* , where we discard all down to second order to reach a Fokker-Planck equation (FPE), in the usual truncation scheme:

$$\begin{aligned} \frac{\partial W^{TBL}}{\partial t} &= \frac{\gamma_{3,1D}}{2} \int dx \left(\frac{\delta}{\delta\psi} \psi + \frac{\delta}{\delta\psi_p^*} \psi^* + 3 \frac{\delta}{\delta\psi} \frac{\delta}{\delta\psi^*} \right) \\ &\times |\psi|^4 W(\psi(x), \psi^*(x), t), \end{aligned} \quad (\text{A7})$$

with TBL indicating that we consider only terms which arise from Eq. (9c).

Since solutions of a FPE directly correspond to those of a stochastic differential equation (SDE), we can solve the former by expressing it using the SDE:

$$d\psi(x) = -\frac{\gamma_{3,1D}}{2} |\psi(x)|^4 \psi dt + \frac{\sqrt{3\gamma_{3,1D}}}{\sqrt{2}} |\psi(x)|^2 d\mathcal{W}(x, t). \quad (\text{A8})$$

Adding the usual terms unrelated to loss [27], we finally reach

$$\begin{aligned} \frac{\partial \psi}{\partial t} &= -\frac{i}{\hbar} \left[-\frac{\hbar^2}{2m} \frac{\partial^2 \psi}{\partial x^2} + V(x) + U_0 |\psi|^2 \right] \psi \\ &- \frac{\gamma_{3,1D}}{2} |\psi|^4 \psi dt + \frac{\sqrt{3\gamma_{3,1D}}}{\sqrt{2}} |\psi|^2 d\mathcal{W}. \end{aligned} \quad (\text{A9})$$

Similar derivations for one- and two-body loss processes yield Eq. (9a) and Eq. (9b).

APPENDIX B: TRUNCATED WIGNER TREATMENT OF CORRELATIONS

As stated before, the TWA allows the sampling of quantum correlations through symmetrically ordered stochastic averages [30,47]. In this Appendix we describe how these can be assembled to infer the correlation function (15) that is central to the present work. The starting point is the association

$$\overline{\psi^*(x)\psi(x')} = \frac{1}{2} (\hat{\Psi}^\dagger(x)\hat{\Psi}(x') + \hat{\Psi}(x')\hat{\Psi}^\dagger(x)), \quad (\text{B1})$$

where the dependence on time has been suppressed since we will deal with equal time correlations only. With the commutation relation $\delta_p(x, x') = [\Psi(x), \Psi^\dagger(x')]$, we obtain

$$\langle \hat{\Psi}^\dagger(x)\hat{\Psi}(x') \rangle = \langle \psi^*(x)\psi(x') \rangle_W - \frac{1}{2} \delta_p(x, x'), \quad (\text{B2})$$

providing already first-order phase correlations $G_1(x, x') = \langle \hat{\Psi}^\dagger(x)\hat{\Psi}(x') \rangle$. Here $\delta_p(x, x')$ is a restricted-basis δ function

given by [30]

$$\delta_p(x, x') = \frac{1}{L} \sum_k [u_k^2 e^{ik(x-x')} - v_k^2 e^{-ik(x-x')}], \quad (\text{B3})$$

where the index k enumerates the finite number of Bogoliubov modes onto which we add noise for the numerical simulation, in Eq. (6). The expression converges to the actual δ function for $k \rightarrow \infty$.

In a similar fashion, we can relate $\langle \hat{\Psi}^\dagger(x)\hat{\Psi}^\dagger(x')\hat{\Psi}(x)\hat{\Psi}(x') \rangle$ with $\overline{\psi^*(x)\psi^*(x')\psi(x)\psi(x')}$. We first write the latter as a symmetric sum of 24 averages containing all the possible permutations of field operators. Each can be brought into the form $\langle \hat{\Psi}^\dagger(x)\hat{\Psi}^\dagger(x')\hat{\Psi}(x)\hat{\Psi}(x') \rangle$ using the commutation relation. After some algebra, we finally obtain

$$\begin{aligned} &\langle \hat{\Psi}^\dagger(x)\hat{\Psi}^\dagger(x')\hat{\Psi}(x)\hat{\Psi}(x') \rangle \\ &= \overline{\psi^*(x)\psi^*(x')\psi(x)\psi(x')} - \frac{1}{2} [\delta_p(x, x') \overline{\psi^*(x)\psi(x')} \\ &+ \delta_p(x', x') \overline{\psi^*(x)\psi(x)} + \delta_p(x, x) \overline{\psi^*(x')\psi(x')} \\ &+ \delta_p(x', x) \overline{\psi^*(x')\psi(x)}] + \frac{1}{4} [\delta_p(x, x)\delta_p(x', x') \\ &+ \delta_p(x, x')\delta_p(x', x)]. \end{aligned} \quad (\text{B4})$$

APPENDIX C: WHITE-HOLE DAMPING

In this Appendix, we describe our implementation of damping on the white hole. For this we add a complex potential

$$V_{\text{damp}}(x) = -i \frac{s}{\hbar} \exp\left(-\frac{(x-x_w)^2}{2\sigma_d^2}\right) (|\psi(x)|^2 - \rho_0) \psi \quad (\text{C1})$$

to the right-hand side of Eq. (1). Here x_w is the location of the white-hole horizon, s the damping strength, and σ_d the width of the damping profile while ρ_0 is as defined in Eq. (6).

One can see that Eq. (C1) causes exponential damping of ψ if the local density at the white hole deviates from the mean value ρ_0 . Since such deviations are integral to unstable modes, the growth of the latter is damped.

APPENDIX D: DIMENSIONALITY REDUCTION

Here we briefly discuss the reduction of the 3D equation of motion to an effective 1D equation. For this purpose, we rewrite the field operator

$$\hat{\Psi}(x, y, z) = \frac{1}{\sqrt{\pi\sigma_y\sigma_z}} e^{-\frac{y^2}{2\sigma_y^2}} e^{-\frac{z^2}{2\sigma_z^2}} \hat{\Psi}(x), \quad (\text{D1})$$

such that transverse excitations are frozen out, using $\sigma_y = \sqrt{\hbar/(m\omega_y)}$, $\sigma_z = \sqrt{\hbar/(m\omega_z)}$, with ω_y and ω_z the trapping

frequencies in the y and z directions, respectively. Defining $\mathcal{N} = \frac{1}{\sqrt{\pi\sigma_y\sigma_z}}$, we obtain that, e.g.,

$$\begin{aligned} & \int_{-\infty}^{\infty} \int_{-\infty}^{\infty} \int_{-\infty}^{\infty} dx dy dz \hat{\Psi}^\dagger(x, y, z) \hat{\rho} \hat{\Psi}(x, y, z) \\ &= \mathcal{N}^2 \pi \sigma_y \sigma_z \int_{-\infty}^{\infty} dx \hat{\Psi}^\dagger(x) \hat{\rho} \hat{\Psi}(x). \end{aligned} \quad (\text{D2})$$

Thus, the 1D master equation for one-body loss is

$$\begin{aligned} \frac{\partial \hat{\rho}}{\partial t} &= \gamma_{1,3D} \int dx [2\hat{\Psi}(x) \hat{\rho} \hat{\Psi}^\dagger(x) \\ &\quad - \hat{\Psi}^\dagger(x) \hat{\Psi}(x) \hat{\rho} - \hat{\rho} \hat{\Psi}^\dagger(x) \hat{\Psi}(x)]. \end{aligned} \quad (\text{D3})$$

Similarly we reach

$$\begin{aligned} \frac{\partial \hat{\rho}}{\partial t} &= \gamma_{2,3D} \mathcal{N}^4 \frac{\pi \sigma_y \sigma_z}{2} \int dx [2\hat{\Psi}(x)^2 \hat{\rho} \hat{\Psi}^\dagger(x)^2 \\ &\quad - \hat{\Psi}^\dagger(x)^2 \hat{\Psi}(x)^2 \hat{\rho} - \hat{\rho} \hat{\Psi}^\dagger(x)^2 \hat{\Psi}(x)^2] \end{aligned} \quad (\text{D4})$$

for two-body loss and

$$\begin{aligned} \frac{\partial \hat{\rho}}{\partial t} &= \frac{\gamma_{3,3D}}{6} \mathcal{N}^6 \frac{(\pi \sigma_y \sigma_z)}{3} \int dx [2\hat{\Psi}(x)^3 \hat{\rho} \hat{\Psi}^\dagger(x)^3 \\ &\quad - \hat{\Psi}^\dagger(x)^3 \hat{\Psi}(x)^3 \hat{\rho} - \hat{\rho} \hat{\Psi}^\dagger(x)^3 \hat{\Psi}(x)^3] \end{aligned} \quad (\text{D5})$$

for three-body loss. At this point we can define effective 1D loss rates

$$\gamma_{1,1D} = \gamma_{1,3D}, \quad (\text{D6})$$

$$\gamma_{2,1D} = \gamma_{2,3D} \frac{\mathcal{N}^4 \pi \sigma_y \sigma_z}{2} = \frac{\gamma_{2,3D}}{2(\pi \sigma_y \sigma_z)}, \quad (\text{D7})$$

$$\gamma_{3,1D} = \gamma_{3,3D} \frac{\mathcal{N}^6 \pi \sigma_y \sigma_z}{3} = \frac{\gamma_{3,3D}}{3(\pi \sigma_y \sigma_z)^2}, \quad (\text{D8})$$

which are used in the main article.

-
- [1] S. W. Hawking, *Commun. Math. Phys.* **43**, 199 (1975).
[2] S. W. Hawking, *Nature (London)* **248**, 30 (1974).
[3] C. Barceló, S. Liberati, and M. Visser, *Living Rev. Relativ.* **8**, 12 (2005).
[4] L. Parker and D. Toms, *Quantum Field Theory in Curved Space-time: Quantized Fields and Gravity*, Cambridge Monographs on Mathematical Physics (Cambridge University Press, Cambridge, UK, 2009).
[5] N. D. Birrell and P. C. W. Davies, *Quantum Fields in Curved Space*, Cambridge Monographs on Mathematical Physics (Cambridge University Press, Cambridge, UK, 1982).
[6] C. Barceló, S. Liberati, and M. Visser, *Class. Quantum Grav.* **18**, 1137 (2001).
[7] L. J. Garay, J. R. Anglin, J. I. Cirac, and P. Zoller, *Phys. Rev. Lett.* **85**, 4643 (2000).
[8] W. G. Unruh, *Phys. Rev. Lett.* **46**, 1351 (1981).
[9] M. Visser, *Class. Quantum Grav.* **15**, 1767 (1998).
[10] C. Barceló, S. Liberati, and M. Visser, *Phys. Rev. A* **68**, 053613 (2003).
[11] J. Steinhauer, *Nat. Phys.* **10**, 864 (2014).
[12] J. Steinhauer, *Nat. Phys.* **12**, 959 (2016).
[13] J. R. M. de Nova, K. Golubkov, V. I. Kolobov, and J. Steinhauer, *Nature (London)* **569**, 688 (2019).
[14] R. Balbinot, A. Fabbri, S. Fagnocchi, A. Recati, and I. Carusotto, *Phys. Rev. A* **78**, 021603(R) (2008).
[15] I. Carusotto, S. Fagnocchi, A. Recati, R. Balbinot, and A. Fabbri, *New J. Phys.* **10**, 103001 (2008).
[16] S. Wüster and C. M. Savage, *Phys. Rev. A* **76**, 013608 (2007).
[17] S. Wüster, *Phys. Rev. A* **78**, 021601(R) (2008).
[18] S. K. Adhikari, *Phys. Rev. A* **71**, 053603 (2005).
[19] M. Ueda and H. Saito, *J. Phys. Soc. Jpn.* **72**, 127 (2003).
[20] H. Saito and M. Ueda, *Phys. Rev. A* **65**, 033624 (2002).
[21] M. W. Jack, *Phys. Rev. Lett.* **89**, 140402 (2002).
[22] S. Wüster and R. El-Ganainy, *Phys. Rev. A* **96**, 013605 (2017).
[23] J. Dziarmaga and K. Sacha, *Phys. Rev. A* **68**, 043607 (2003).
[24] U. Leonhardt, *Ann. Phys.* **530**, 1700114 (2018).
[25] M. Isoard and N. Pavloff, *Phys. Rev. Lett.* **124**, 060401 (2020).
[26] J. Steinhauer, [arXiv:2110.06796](https://arxiv.org/abs/2110.06796).
[27] M. J. Steel, M. K. Olsen, L. I. Plimak, P. D. Drummond, S. M. Tan, M. J. Collett, D. F. Walls, and R. Graham, *Phys. Rev. A* **58**, 4824 (1998).
[28] A. Sinatra, C. Lobo, and Y. Castin, *Phys. Rev. Lett.* **87**, 210404 (2001).
[29] A. Sinatra, C. Lobo, and Y. Castin, *J. Phys. B: At. Mol. Opt. Phys.* **35**, 3599 (2002).
[30] P. Blakie, A. Bradley, M. Davis, R. Ballagh, and C. Gardiner, *Adv. Phys.* **57**, 363 (2008).
[31] S. Wüster, B. J. Dąbrowska-Wüster, S. M. Scott, J. D. Close, and C. M. Savage, *Phys. Rev. A* **77**, 023619 (2008).
[32] C. Mayoral, A. Recati, A. Fabbri, R. Parentani, R. Balbinot, and I. Carusotto, *New J. Phys.* **13**, 025007 (2011).
[33] M. Tettamanti, S. L. Cacciatori, A. Parola, and I. Carusotto, *Europhys. Lett.* **114**, 60011 (2016).
[34] J. R. M. de Nova, S. Finazzi, and I. Carusotto, *Phys. Rev. A* **94**, 043616 (2016).
[35] P.-E. Larré, A. Recati, I. Carusotto, and N. Pavloff, *Phys. Rev. A* **85**, 013621 (2012).
[36] Y.-H. Wang, T. Jacobson, M. Edwards, and C. W. Clark, *SciPost Phys.* **3**, 022 (2017).
[37] S. Weinfurter, E. W. Tedford, M. C. J. Penrice, W. G. Unruh, and G. A. Lawrence, *Phys. Rev. Lett.* **106**, 021302 (2011).
[38] L.-P. Euvé, F. Michel, R. Parentani, T. G. Philbin, and G. Rousseaux, *Phys. Rev. Lett.* **117**, 121301 (2016).
[39] L.-P. Euvé, S. Robertson, N. James, A. Fabbri, and G. Rousseaux, *Phys. Rev. Lett.* **124**, 141101 (2020).
[40] M. J. Jacquet, S. Weinfurter, and F. König, *Philos. Trans. R. Soc. A* **378**, 20190239 (2020).
[41] T. c. v. Opatrný, M. Kolář, and K. K. Das, *Phys. Rev. A* **91**, 053612 (2015).
[42] L. Mathey, A. Ramanathan, K. C. Wright, S. R. Muniz, W. D. Phillips, and C. W. Clark, *Phys. Rev. A* **82**, 033607 (2010).
[43] C. J. Pethik and H. Smith, *Bose-Einstein Condensation in Dilute Gases* (Cambridge University Press, Cambridge, UK, 2002).
[44] L. J. Garay, J. R. Anglin, J. I. Cirac, and P. Zoller, *Phys. Rev. A* **63**, 023611 (2001).
[45] S. Finazzi and R. Parentani, *New J. Phys.* **12**, 095015 (2010).

- [46] A. Sinatra and Y. Castin, *Eur. Phys. J. D* **4**, 247 (1998).
- [47] A. A. Norrie, R. J. Ballagh, C. W. Gardiner, and A. S. Bradley, *Phys. Rev. A* **73**, 043618 (2006).
- [48] S. Giovanazzi, C. Farrell, T. Kiss, and U. Leonhardt, *Phys. Rev. A* **70**, 063602 (2004).
- [49] M. Tettamanti, S. L. Cacciatori, and A. Parola, *Phys. Rev. D* **99**, 045014 (2019).
- [50] M. J. Jacquet and F. Koenig, *SciPost Phys. Core* **3**, 005 (2020).
- [51] See Supplemental Material at <http://link.aps.org/supplemental/10.1103/PhysRevA.106.053317> for movies of the dynamics from simulations as shown in Fig. 2.
- [52] G. R. Dennis, J. J. Hope, and M. T. Johnsson, *Comput. Phys. Commun.* **184**, 201 (2013).
- [53] M. Naraschewski and R. J. Glauber, *Phys. Rev. A* **59**, 4595 (1999).
- [54] I. Carusotto, R. Balbinot, A. Fabbri, and A. Recati, *Eur. Phys. J. D* **56**, 391 (2010).
- [55] P. Jain, S. Weinfurter, M. Visser, and C. W. Gardiner, *Phys. Rev. A* **76**, 033616 (2007).
- [56] Note that a real equilibrium cannot be reached, since the BEC keeps losing atoms. We use $c(t^*)$ to evaluate T_{loss} .
- [57] S. Corley and T. Jacobson, *Phys. Rev. D* **59**, 124011 (1999).
- [58] S. Corley and T. Jacobson, *Phys. Rev. D* **54**, 1568 (1996).
- [59] C. Barceló, A. Cano, L. J. Garay, and G. Jannes, *Phys. Rev. D* **74**, 024008 (2006).
- [60] M. Tettamanti, I. Carusotto, and A. Parola, *Europhys. Lett.* **133**, 20002 (2021).
- [61] J. Söding, D. Guéry-Odelin, P. Desbiolles, F. Chevy, H. Inamori, and J. Dalibard, *Appl. Phys. B* **69**, 257 (1999).
- [62] M. Isoard, Ph.D. thesis, Université Paris-Saclay, 2020, <https://tel.archives-ouvertes.fr/tel-02974737>.
- [63] A. Finke, P. Jain, and S. Weinfurter, *New J. Phys.* **18**, 113017 (2016).
- [64] A. Peres, *Phys. Rev. Lett.* **77**, 1413 (1996).
- [65] M. Horodecki, P. Horodecki, and R. Horodecki, *Phys. Rev. Lett.* **78**, 574 (1997).
- [66] X. Busch and R. Parentani, *Phys. Rev. D* **89**, 105024 (2014).
- [67] M. Isoard, N. Milazzo, N. Pavloff, and O. Giraud, *Phys. Rev. A* **104**, 063302 (2021).
- [68] J. R. M. de Nova, F. Sols, and I. Zapata, *New J. Phys.* **17**, 105003 (2015).
- [69] J. Steinhauer, *Phys. Rev. D* **92**, 024043 (2015).
- [70] D. Boiron, A. Fabbri, P.-E. Larré, N. Pavloff, C. I. Westbrook, and P. Ziñ, *Phys. Rev. Lett.* **115**, 025301 (2015).
- [71] A. Pendse, S. Shirol, S. Tiwari, and S. Wüster, *Phys. Rev. A* **102**, 053322 (2020).
- [72] H. S. Nguyen, D. Gerace, I. Carusotto, D. Sanvitto, E. Galopin, A. Lemaître, I. Sagnes, J. Bloch, and A. Amo, *Phys. Rev. Lett.* **114**, 036402 (2015).
- [73] D. Gerace and I. Carusotto, *Phys. Rev. B* **86**, 144505 (2012).
- [74] D. D. Solnyshkov, H. Flayac, and G. Malpuech, *Phys. Rev. B* **84**, 233405 (2011).
- [75] M. J. Jacquet, L. Giacomelli, Q. Valnais, M. Joly, F. Claude, E. Giacobino, Q. Glorieux, I. Carusotto, and A. Bramati, [arXiv:2110.14452v2](https://arxiv.org/abs/2110.14452v2).